Full length article

# Extended defects in 3C-SiC: Stacking faults, threading partial dislocations, and inverted domain boundaries

Massimo Zimbone [a,*], Andrey Sarikov [b,c], Corrado Bongiorno [d], Anna Marzegalli [e], Viviana Scuderi [d], Cristiano Calabretta [d], Leo Miglio [b], Francesco La Via [d]

[a] IMM-CNR, V. S. Sofia 24, Catania 95128, Italy
[b] L-NESS and Dipartimento di Scienza dei Materiali, Università degli Studi di Milano-Bicocca, via R. Cozzi 55, Milano 20125, Italy
[c] V. Lashkarev Institute of Semiconductor Physics NAS Ukraine, 45 Nauki avenue, Kyiv 03028, Ukraine
[d] IMM-CNR, VIII Strada, 5, Catania 95121, Italy
[e] L-NESS and Dipartimento di Fisica, Politecnico di Milano, via Anzani 42, Como 22100, Italy

## ARTICLE INFO

## ABSTRACT

The presence of extended bi-dimensional defects is one of the key issues that hinder the use of wide band-gap materials hetero-epitaxially grown on silicon. In this work, we investigate, by STEM measurements and molecular dynamic simulations, the structure of two of the most important extended defect affecting the properties of cubic silicon carbide, 3C-SiC, hetero-epitaxially grown on (001) silicon substrates: (1) stacking faults (SFs) with their bounding threading dislocation arms, even along with unusual directions, and (2) inverted domain boundaries (IDBs). We found that these two defects are strictly correlated: IDBs lying in {111} planes are intrinsically coupled to one or more SFs. Moreover, we observed that threading partial dislocations (PDs), limiting the SFs, appear to have non-conventional line directions, such as [112], [123], and [134]. Molecular dynamics simulations show that [110] and [112] directions allow for stable dislocation structures, while in the unusual [123] and [134] directions, the PDs are composed of zig-zag dislocation lines in the [112] and [110] directions.

© 2021 Published by Elsevier Ltd on behalf of Acta Materialia Inc.

## 1. Introduction

Despite the great efforts of the scientific community, the quality of many wide band-gap semiconductors grown on silicon substrates is still limited by the presence of extended defects, which hinder their use in the microelectronic industry. 3C-SiC is a very interesting material, [1] not only for electronic applications. Indeed, it has a number of properties that allow to use it in new emerging fields, such as photocatalysis, water splitting, or for biological applications [2–11]. As compared to the mostly used 4H-SiC polytype, 3C-SiC has higher bulk and channel electron mobility (up to 1000 and 250 cm$^2$ V$^{-1}$ s$^{-1}$, respectively) [7–9] and lower trap density at the oxide-semiconductor interface (3C-SiC/SiO$_2$) [8,9,12]. The use of 3C-SiC polytype, instead of 4H-SiC, can boost the transition to a green economy. 3C-SiC based MOSFET devices (working

in the range of breakdown voltages below 1200 V) can be used to drive power electric vehicles, air conditioning, and LED lighting systems [13,14]. It will be possible because the 3C-SiC polytype is stable at temperatures below the melting temperature for silicon, meaning that it can be grown on silicon substrates, reducing considerably the cost of the SiC wafer production. It also reduces considerably the power dissipation with respect to 4H-SiC in this range of breakdown voltage.

Despite the promising importance of 3C-SiC material for semiconductor applications, as well as more than 30 years of studies on it, the problem of the 3C-SiC hetero-epitaxy on silicon is far from being solved [15]. The most important issues are related to the presence of 2D extended defects in the epitaxial layers. Stacking Faults (SFs), along with the partial dislocations (PDs), together with inverted domain boundaries (IDBs) are the most important 2D extended defects in 3C-SiC films, grown hetero-epitaxially on (001) Si substrates. Notwithstanding the importance of the extended 2D defects on the electrical and mechanical properties of the 3C-SiC, only a limited number of papers describe the fine structure of such defects

The IDBs are the most important 2D extended defects affecting the properties of 3C-SiC grown on "on-axis" (001) Si wafers. They

* Corresponding author.
*E-mail addresses:* massimo.zimbone@imm.cnr.it, massimo.zimbone@ct.infn.it (M. Zimbone), andrey.sarikov@unimib.it (A. Sarikov), Corrado.Bongiorno@imm.cnr.it (C. Bongiorno), anna.marzegalli@unimib.it (A. Marzegalli), Viviana.Scuderi@imm.cnr.it (V. Scuderi), cristiano.calabretta@imm.cnr.it (C. Calabretta), leo.miglio@mater.unimib.it (L. Miglio), francesco.lavia@imm.cnr.it (F. La Via).

are related to the formation of crystallographic domains [16–18]. These defects nucleate due to two different configurations of the Si-C dimers on the surface: Si-C dimers can be arranged in two perpendicular alignments. Owing to crystal symmetry, rotation by 90° around [001] is equivalent to flipping the crystal upside down (i.e. rotation by 180° around [110]). In literature, IDBs are called also anti-phase boundaries (APB) [14,17]. IDBs cause the electrical failure of 3C-SiC/(001) Si-based devices [19–22]. Current maps in the nano-scale range obtained by conductive atomic force microscopy showed that IDBs are the main defects responsible for the short circuit, under both reverse and forward bias polarization [20]. Recently, high-resolution STEM images of the IDBs, lying in the {110} planes, revealed that they are coherent, have no polar character, and are composed of distorted Si-C bonds, forming a square and a semi-octahedral structure with undistorted bonds [22]. To the best knowledge of us, no structure of the IDBs in the planes other than {110} was reported so far in SiC.

Hetero-epitaxial growth of 3C-SiC on (001) Si suffers from two main issues: interfacial lattice mismatch between Si and SiC and the difference in thermal expansion coefficients. These two issues lead to the formation of misfit and Lomer dislocations at the hetero-interface [23] and the presence of local strain field within the epilayer. The presence of domain boundaries together with the residual stress (as well as other minor factors such as e. g. dopant segregation) can drive the formation of both perfect and partials dislocations (together with SFs) in the epilayer, and disconnections in the IDBs [24–29]. For sake of clarity, we can recall that disconnections are topological line defects constrained to crystalline interfaces with both step and dislocation character and we also recall that SFs consist of a wrong stacking order with respect to the 3C-SiC one [28–36] (for insights, and definitions the reader can refer to Ref. [27]). The SFs, being generated at the interface, are able to propagate into the SiC epilayer toward the surface and greatly affect the mechanical and electrical properties of the material. In particular, it was recently demonstrated by conductive-AFM that SFs act as preferential current paths under forward polarization [19]. SF is bordered by two PDs, which limit the wrong sequence plane from the perfect 3C sequence regions. It has been also demonstrated recently that the dislocation complexes bounding multiple SFs generate intra-gap electronic states in the materials causing leakage currents [20]. The shape, direction, and stability of PDs bounding the SFs are of particular importance because the expansion or the shrinking of SFs is driven by the energetics and kinetics of the PDs [37,38]. It was also demonstrated that for other SiC poly-types (4H-SiC), the shape of SFs is influenced by the mobility of the PDs, and mobility is notably influenced by the core structure (which can be either of Si- or C-type) of the dislocation [39]. Moreover, the expansion of SFs due to the gliding of PDs leads to their intersections and the formation of other types of dislocations, such as Lomer-Cottrell locks and "forest" dislocations [31].

In this work, we experimentally study the 2D defects in 3C-SiC layers hetero-epitaxially grown on (001) Si substrates by using high-resolution scanning transmission electron microscopy (STEM). The nature of IDB allows us to obtain atomic images of the fine structure of the boundary with high resolution (lower than Å) and to correlate the SFs with IDBs. PDs are observed at low magnification, and the line directions of the PDs threading the epilayer are found to be different from the expected ones, as predicted by the standard theory of dislocations. Therefore, we investigate by molecular dynamics the stability and the structure of the PDs.

## 2. Material and methods

3C-SiC was grown hetero-epitaxially using chemical vapor deposition (CVD), in a horizontal hot-wall reactor at the LPE industry. The (001) Si substrate was a 4 inch 350 μm thick wafer. Hydrogen ($H_2$) was used as a carrier gas. Before the growth, the Si substrate underwent a carbonization step at 1100°C by introducing ethylene [40]. The CVD growth process was performed at a pressure and temperature of $10^4$ Pa and 1370°C, respectively. The gases used during the growth were trichlorosilane (TCS) and ethylene ($C_2H_4$) as silicon and carbon precursors, respectively [41,42]. At the applied experimental conditions, only the 3C phase was detected in the hetero-epitaxial layer on Si, and the final 3C-SiC thickness was 30 μm.

Scanning Transmission Electron Microscopy (STEM) was carried out on a JEOL ARM200F probe Cs-corrected TEM, equipped with a cold FEG and working at 200 kV. We operated with three detectors, acquiring three images contemporaneously: at low, medium, and high scattering angles. We follow the defects from the low magnification to the high resolution. Low angle detector allows us to have Bright Field (BF) images while the High Angle Annular Dark Field (HAADF) detector (with an inner semi-angle of 80 mrad) was used to obtain the dark-field STEM images. In this configuration the signal in the image is mainly related to the atomic number Z, allowing a direct identification of the carbon and silicon atomic columns at the distance of 1.1 Å each other. The images were exported by using the Digital Micrograph Software and analyzed with ImageJ software. We used ImageJ tools to denoise, smooth, and modify the contrast of the images.

Images in "plane view" were acquired with a JEOL JEM2010F in TEM mode. Diffraction contrast was used in standard and two-beam configuration for the study of the SFs and PDs.

Molecular dynamics simulations of the evolution of PDs in the 3C-SiC layers were performed using the Large-scale Atomic/Molecular Massively Parallel Simulator (LAMMPS) code [43]. Dislocation dipoles consisting of two PDs with opposite Burgers vectors, separated by a stacking fault, were inserted in the $(1\bar{1}1)$ plane of the simulation cells, by shifting all the atoms in the simulation cell by the displacement vectors according to the dislocation theory [36]. Periodic boundary conditions were applied in all three directions of the simulation cell. The annealing was performed at the simulation temperature of 2000 K in the Nose-Hoover thermostat regime during 15 ps. The time step was equal to 0.3 fs, ensuring energy conservation during the simulation runs. To avoid the influence of the SF energy in the evolution of dislocation dipoles, analytical bond order potential (ABOP) was chosen for MD simulations [44]. This potential is parameterized in such a way that only the interactions of nearest-neighbor atoms are taken into account. Therefore, ABOP makes no difference in energy between various SiC polytypes and the SF energy is equal to zero. Still, ABOP enables a more correct description of the dislocation core configurations, as compared to other empirical potentials [45]. Analysis of the dislocation structures in the next section was performed with the OVITO or VESTA software [46,47].

## 3. Results and discussion

### 3.1. Stacking faults structure

The 3C-SiC has a zinc-blend crystallographic structure and SFs lie always in the {111} planes [35,36]. In low magnification and (110) projected TEM images, SFs can appear either as straight lines or having trapezoidal shapes, as considered below. Two of the four {111} planes (namely the $(1\bar{1}1)$ and the $(\bar{1}11)$ ones) are perpendicular to the (110) observation plane, as shown in the upper part of Fig. 1, and they appear as straight lines. On the contrary, SFs that lie in the (111) and $(\bar{1}\bar{1}1)$ planes intersect the TEM lamellae faces and are trapezoidal in shape. One of such SFs is shown in the upper part of Fig. 1 as well. In this image, it is also possible to see the PDs, highlighted in red, that border the SF to the perfect
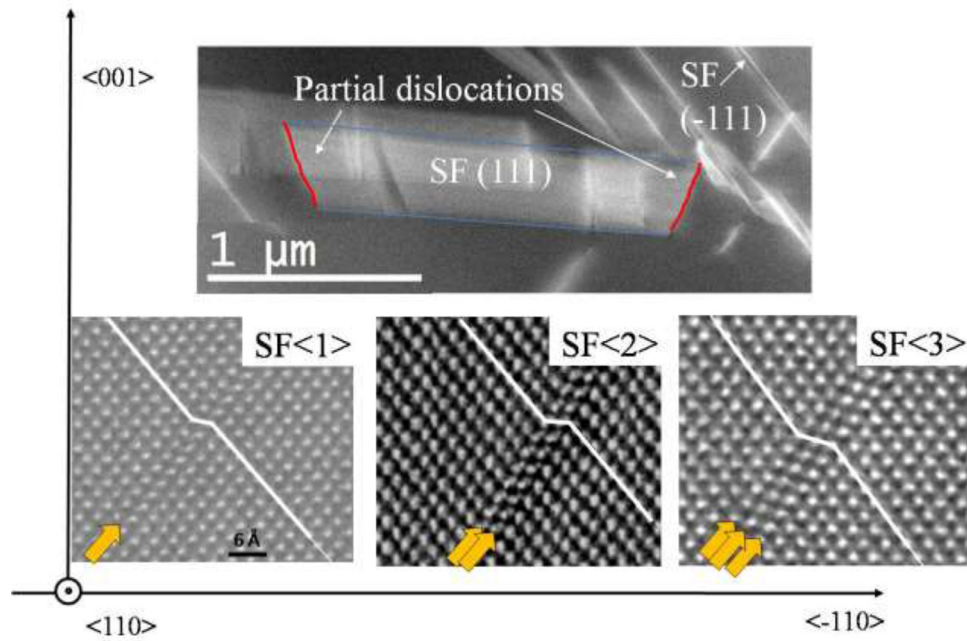
**Fig. 1.** Cross-section TEM image of the 3C-SiC layer in the (110) projection. Top part: SFs lying in the (-111) plane appear as lines tilted 45° off, while SFs lying in the (111) plane are visible as trapezoidal-shaped. PDs at the SF edges are shown in red while the intersections of the SF with the TEM lamellae are indicated by light blue lines.Bottom part: HAADF-STEM images showing the three kinds of SFs observed in 3C-SiC. They consist of 1, 2, or 3 faulted atomic layers. The SF faulted layers are indicated with yellow arrows while the white lines are drawn as guides for eyes. Marker is the same for all three images. (For interpretation of the references to color in this figure legend, the reader is referred to the web version of this article.)

3C-SiC crystal. The SF intersections with the lamella surfaces are evidenced by light-blue lines.

SFs detected in the 3C-SiC can belong to one of the three types, depending on the number of atomic planes with the wrong orientation of the Si–C dimers (with respect to the perfect crystal) they contain [20,22,23]. Namely, SF<1>, SF<2>, and SF<3> are made up of one, two or three faulted atomic layers, and are called intrinsic, extrinsic, and conservative SFs, respectively [20,22,23]. In the lower part of Fig. 1, all the three SF types are shown in the cross-view HR-STEM images in the lower panels of the figure. The yellow arrows indicate the faulted atomic planes.

Fig. 2 a–e shows a series of images of SFs (lying in the (111) plane), in projection onto the (001) plane (plane view). The SFs intersect the upper and the lower part of the TEM lamellae by the lines in the $\langle \bar{1}10 \rangle$ direction that are marked as the black dotted lines. Let's consider first the SF presented in Fig. 2a. PDs bounding this SF to the not-faulted 3C-SiC crystal are marked by white dotted lines. One of the PDs is vertical and the other one is horizontal, having projected coordinates <0,1> and <1,0>, respectively. If they are considered in 3D space, these dislocations lie in the (111) plane: thus, the three-dimensional vector coordinates of their lines are easily calculated to be $\langle 01\bar{1} \rangle$ for the vertical PD and $\langle 10\bar{1} \rangle$ for the horizontal PD, respectively. Following the same considerations, the coordinates of the line vectors for all the PDs found in Fig. 2 can be calculated. For easy recognition of the projected directions onto the (001) plane, we draw the arrows corresponding to the directions <1,3>, <1,2>,<1,1>, <2,1>, and <3,1> in the bottom-left part of Fig. 2. In Fig. 2b, two white dotted lines indicating the SF bounding PDs, have the projections in the directions <2,1> and <1,1>. It means that their three-dimensional line vectors are $\langle 21\bar{3} \rangle$ and $\langle 11\bar{2} \rangle$ respectively. In Fig. 2c, PDs lines lie in the directions $\langle 12\bar{3} \rangle$ and $\langle 21\bar{3} \rangle$, while in Fig. 2d and e in the directions $\langle 13\bar{4} \rangle$, $\langle 11\bar{2} \rangle$ and $\langle 10\bar{1} \rangle$. Based on the results of experimental observations here presented, it is apparent that the dislocations are characterized by peculiar families of line directions, which are [110] as well as [112], [123] and [134]. For the sake of scientific

rigor, we can note here that some of the PDs showed in Fig. 2 are blurry (especially those aligned in the [123] or [134] line directions). They can be considered straight only roughly and (as it will be shown in the next) they can be composed by smaller segments.

Let's consider a particular SF, for example, Fig. 3a reports the bright-field TEM images of an isolated one. In this figure, white lines are parallel to the PDs lines and the brace individuates the position of the SF. Note that the dislocation line on the left is parallel to $\langle 11\bar{2} \rangle$ direction while the PD on the right is composed of two linear segments parallel to $\langle 10\bar{1} \rangle$ and $\langle 11\bar{2} \rangle$ directions, respectively. Now, we wonder if a correlation exists between unusual PD directions (in this case $\langle 11\bar{2} \rangle$) and the Burgers vector of the PDs. The information on the Burgers vectors of the PDs can be obtained using TEM images in the two-beam configuration i.e. by selecting the transmitted beam and another beam with defined scattering vector $\mathbf{g}$, also using the so-called invisibility criterion. The invisibility criterion states that when the scattering vector $\mathbf{g}$ is perpendicular to the Burgers vector of the dislocation (or the translation vector of the SF), the dislocation (or SF) has very low contrast, so it becomes invisible [48]. In Fig. 1 S.I., we report the diffraction pattern of the crystal of Fig. 3 together with the scattering vectors $\mathbf{g1}$, $\mathbf{g2}$, and $\mathbf{g3}$. These vectors individuate the spots used in the two-beam configuration analyses. In Fig. 2.S.I.–5.S.I. some images of the sample, acquired by using the bright field (Fig. 2 S.I.) and the $\mathbf{g1}$ (Fig. 3 S.I.), $\mathbf{g2}$ (Fig. 4 S.I.), and $\mathbf{g3}$ (Fig. 5 S.I.) vectors in a two-beam configuration are presented; the direction of the vector $\mathbf{g}$ is indicated by a red arrow. Now, we focus our attention on the particular SF observed in Fig. 3. The image in Fig. 3b is taken in the same region as Fig. 3a, using the two-beam configuration. We considered the transmitted beam and the $\langle 2\bar{2}0 \rangle$ diffracted beam (i.e. the vector $\mathbf{g2}$ of Fig. 1 S.I.). In this image, only the PD on the left (in the $\langle 11\bar{2} \rangle$ direction) can be seen, while both SF and PD on the right have very low contrast, i.e. the invisibility criterion is fulfilled.

Let's now discuss these findings as follows. In Fig. 3b, the SF disappears because the $\mathbf{g2}$ vector ($\langle 2\bar{2}0 \rangle$) is perpendicular to one of the equivalent translation vectors of the SF, namely $\langle 11\bar{2} \rangle$, so the SF
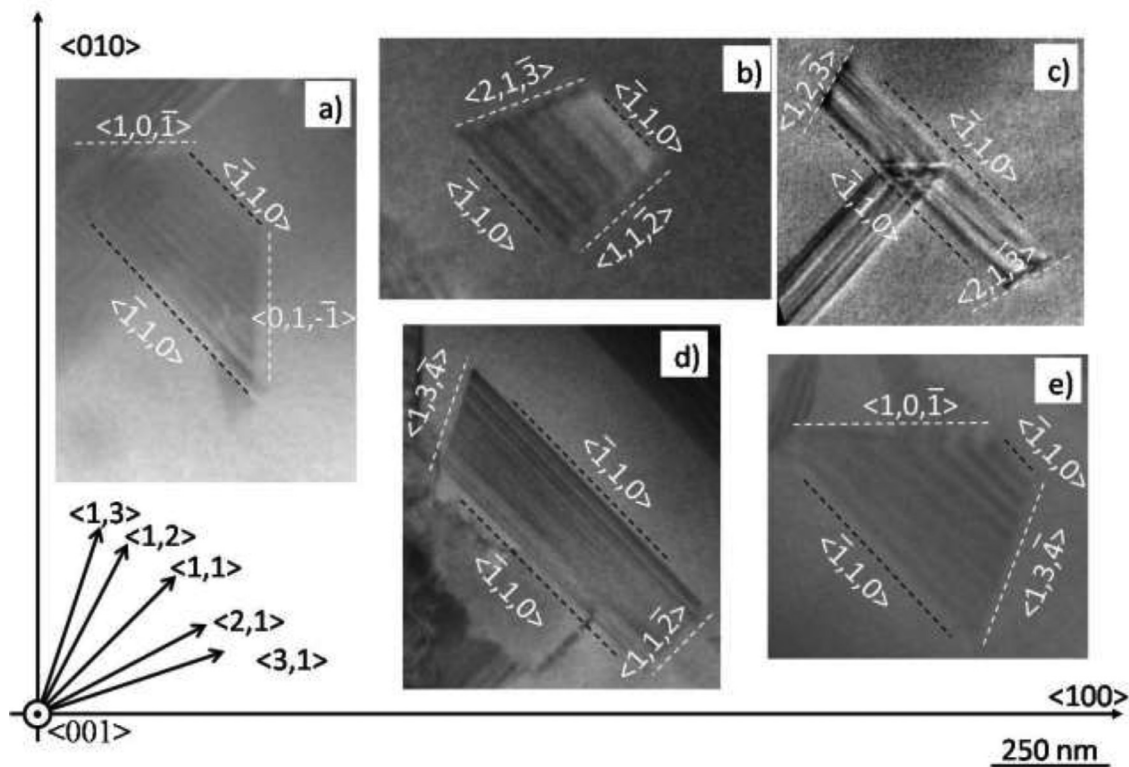
**Fig. 2.** Low-resolution plane view of several SFs laying on $(1\bar{1}1)$ plane. The intersection between SF and TEM lamellae and PD, limiting the SF, are highlighted with dotted black and white lines respectively. Directions of the white and black lines are also reported in the figures. On the left down the axis and some important directions projected on the (001) plane are drawn for easy recognition of the PD direction. Marker is the same for all the figures.

becomes invisible according to the invisibility criterion. The invisibility of the PD on the right in Fig. 3b means that its Burgers vector is perpendicular to the vector **g2**. Moreover, PDs in the (111) plane (of an FCC crystal as 3C-SiC) can have only one of the three Burgers vectors as follows: $1/6\langle11\bar{2}\rangle$, $1/6\langle\bar{2}11\rangle$, or $1/6\langle1\bar{2}1\rangle$ [35]. These vectors are drawn in the left-bottom part of Fig. 3. From the above considerations, it is easy to state that the Burgers vector of the PD on the right is $1/6\langle11\bar{2}\rangle$ (perpendicular to **g2**). The angle between the dislocation segments (that compose the dislocation on the right) and the Burgers vector is 30° for $\langle10\bar{1}\rangle$ segment and 0° for the $\langle11\bar{2}\rangle$ segment. We highlight that the latter PD segment has a screw character. On the contrary, the PD on the left is visible as a dotted small curved line. It means that its Burgers vector is not perpendicular to the **g2** vector. It can have either $1/6\langle\bar{2}11\rangle$ or $1/6\langle1\bar{2}1\rangle$ direction. Unfortunately, we are not able to distinguish between these two possibilities, but, in both cases, the Burgers vector of the PD is tilted by 60° with respect to the line direction $\langle11\bar{2}\rangle$, i.e. PD on the left has both edge and screw components.

Fig. 3c, provides a schematic representation of the SF together with the dislocation lines and their Burgers vectors: white and blue lines show PDs lines and Burgers vectors, respectively. The angles between the dislocation line directions and the Burgers vectors are also presented in this image. The PD on the left is shown to have a Burgers vector $1/6\langle\bar{1}2\bar{1}\rangle$ and direction of the dislocation line $\langle11\bar{2}\rangle$, with the angle of 60° between them (different from the typical angle of 30 or 90° [35]). The PD on the right has the Burgers vector $1/6\langle11\bar{2}\rangle$ and is composed of two segments tilted 30° ($\langle10\bar{1}\rangle$) and 0° ($\langle11\bar{2}\rangle$) with respect to the dislocation line direction. In this case, the presence of $\langle11\bar{2}\rangle$ line segment can be favored by its screw character, having smaller line energy, as compared to the edge dislocation. In further analyses, we observed angles lower than 30° for line dislocations in the unusual [123] and [134] line directions.

The peculiar dislocation line directions have to be the result of the minimization of the dislocation energy. In order to discuss the formation of particular line directions observed experimentally, we recall here the principal rules that determine the PD line directions [35,36]: (1) a dislocation tends to be as short as possible, thus minimizing its self-energy and 2) a dislocation "runs" in the minima of the Peierls potential, i.e. it tends to align along with the specific preferred low-energy directions. These two rules indicate that PDs in 3C-SiC crystals should preferably align in the <110> directions, always favorable in FCC lattices [35]. Moreover, the direction of the Burgers vector could also influence the PD line direction. Indeed, the third rule for the direction of the dislocation line states that a dislocation tends to have a screw component as larger as possible since the self-energy per unit length of a screw dislocation is smaller than that of an edge dislocation. So, it is possible to understand that the dislocation lines are straight (following the first rule) and some of these PD lines lie on [110] and [112] (second rule) directions. However, these rules are unable to explain the experimental TEM images shown in Fig. 2 b–e, where [132] and [143] line directions are observed.

To better understand the formation of the "weird" PDs line directions, we have studied the stability of PDs with [132] and [143] line directions using MD simulations. Fig. 4 shows the transformation of the dislocation line (shown in green color), initially in the <132> direction, as the result of the simulated annealing at 2000 K during 15 ps. Analogous results for the <143> direction of the dislocation line are presented in Fig. 6 S.I. It can be seen from these figures that the dislocation lines under study are not stable and evolve during annealing. In particular, both of them acquire a zigzag shape, made out of segments aligned in the <011> direction (known to be the preferential ones for PDs, from the crystallographic point of view), in alternation with the segments aligned in the <121> direction, favored by their screw nature with a smaller
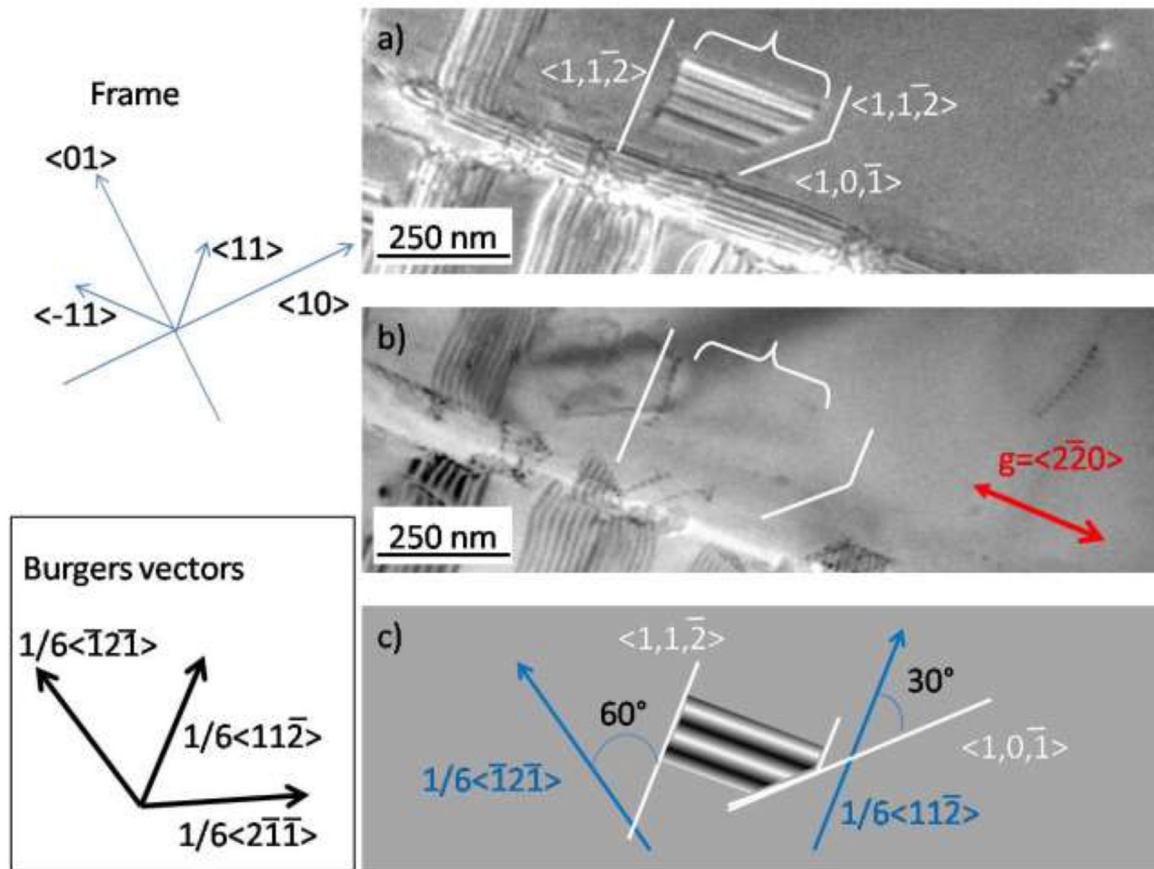
**Fig. 3.** (a) Bright-field images of SFs. (b) Two-beam image obtained in the same region of figure a. The **g** vector used for image contrast is indicated by a red arrow. (c) Schematic representation of SF with dislocation lines, Burgers vectors, and angles between the two. White lines are parallel to the PD lines, brace individuates the position of the SF. They are drawn as a guide for the eye. Blue arrows are the Burgers vector of the PDs. PD Burgers vectors direction allowed in an FCC crystal are also reported on the left down part of the figure. (For interpretation of the references to color in this figure legend, the reader is referred to the web version of this article.)
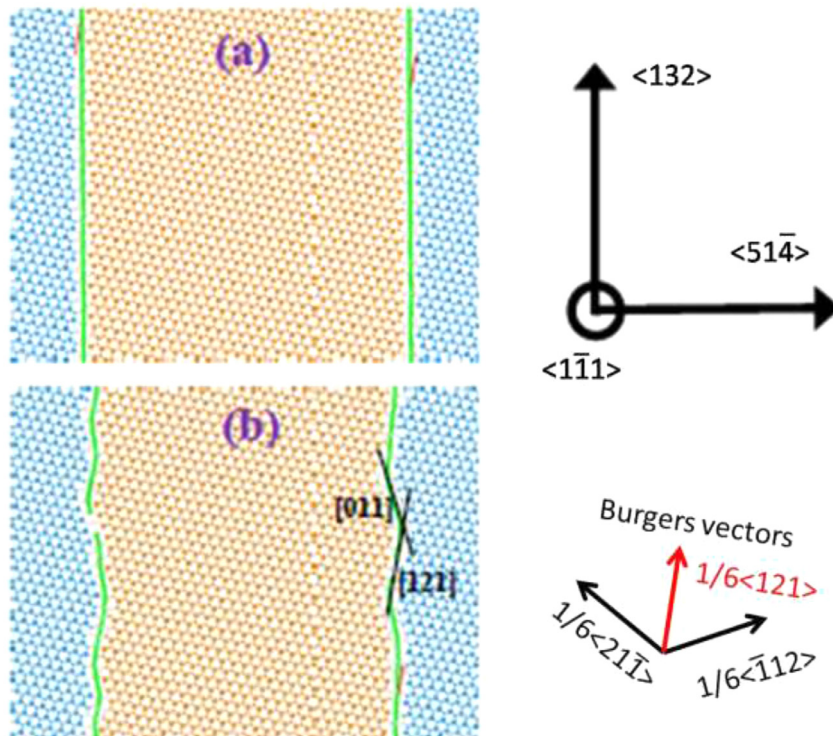


**Fig. 4.** MD simulated evolution of the PD with dislocation lines along the <132> direction: a) before annealing b) after annealing. Burgers vectors are drawn in the right down part of the figure. The particular Burgers vector used in the simulation (1/6<121>) is highlighted in red. (For interpretation of the references to color in this figure legend, the reader is referred to the web version of this article.)
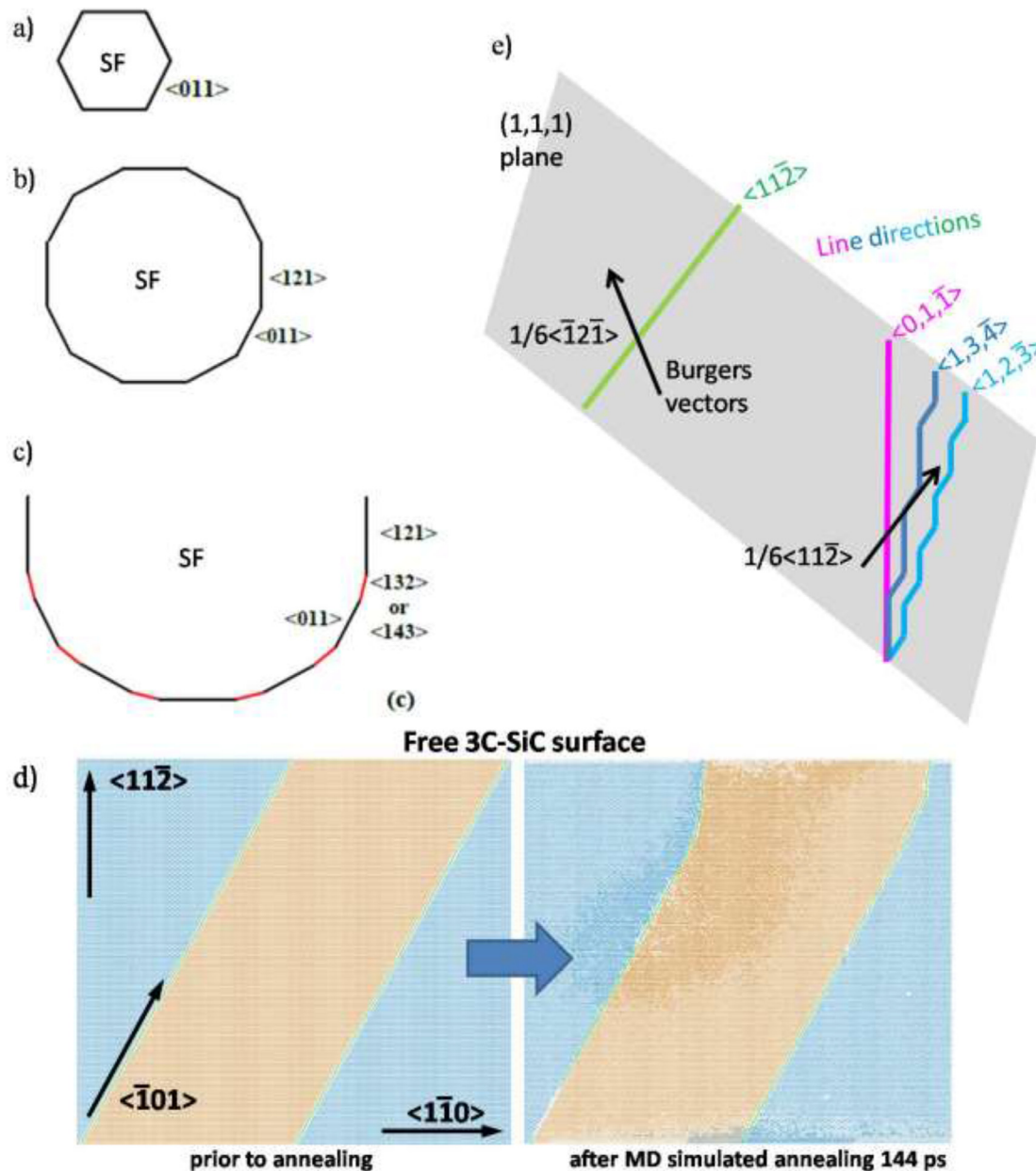
**Fig. 5.** (a-c) Scheme of the evolution of the PD loop with different sizes. For small size (a), only [110] direction lines are observed while for larger size (b) also [112] directions appear. For very large size (c) [132] and [143] directions (highlighted in red) appear. Panel (d) presents the MD simulated snapshots of the change of the dislocation line direction from the preferential <110> to the <112> one as a result of energy minimization by shortening the dislocation length near the free surface. Blue atoms represent the atoms in the 3C-SiC zinc-blend structure, orange color refers to the stacking fault, and green lines are the lines of the Shockley PDs. e) a representation of the configurations found in Figs. 2 is drawn: PDs on the plane (111) are colored magenta, green, dark, and light blue. (110) black lines are the intersections of the (111) plane with the lamellae faces (almost (001) plane). Black arrows are the Burgers vectors in the (111) plane. Note that blue lines (dark and light) have a zig-zag shape as it is discussed in the text. (For interpretation of the references to color in this figure legend, the reader is referred to the web version of this article.)

self-energy, as compared to other directions. We may conclude, therefore, that the observed dislocation lines oriented along <132> (and <143>) directions are, actually, the convolution of step-like lines formed by the segments <011> and <121>. In particular, the effective <132> segment of the PD line is formed by one <011> plus one <121> segment, while the <143> segment by one <121> plus "two" <011> segments, respectively.

We can discuss how the appearance of the visible <132> and <143> alignments of the dislocation line (actually consisting of the <011> and <121> segments as shown above) may influence the shortening during loop and semiloop extension. In Fig. 5 a–c, we consider the evolution of a PD loop enclosing an SF in the 3C-SiC film. A small initial loop is expected to be formed by six

segments aligned in the equivalent [011] directions, corresponding to the preferential directions of the dislocation line (see Fig. 5a). Increasing the loop size, we expect an increase in its energy due to the elongation of the dislocation line. At a certain size of the loop, it should become energetically favorable to shorten the dislocation length by the formation of segments with different alignments with respect [011] and somewhat higher line energy. Based on the results described above, these new alignments should be along with equivalent [112] directions. The loop shape changes (see Fig. 5 b), and the formation of the step-like configurations made up by the [011] and [112] line segments is possible. A larger loop induces the formation of [132] and [143] directions (see Fig. 5c), as observed experimentally. Moreover, when the loop reaches the
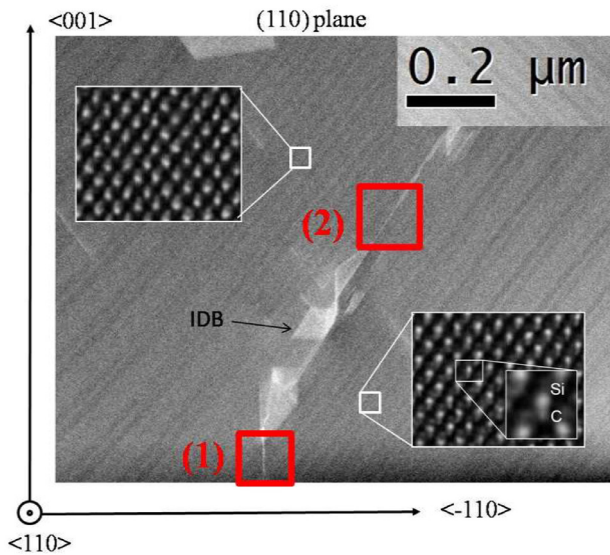
**Fig. 6.** Low-resolution cross-section STEM image of an IDB projected on the (110) plane. The regions in which the IDB is perpendicular to the observation plane (110) are highlighted as the region (1) and region (2). In the insets, high-resolution HAADF-STEM images of the Si-C dimer are displayed. Note that Si and C dimer is reversed upside down in the two insets.

surface it becomes a semi loop with threading arms extending throughout the layer. The presence of the free surface, by the action of the image force, allows the threading arms to further decrease their lengths upon a change in their direction towards the direction corresponding to the projection of the free surface normal line in the glide direction. This change can be exploited via the insertion of segments [121], which may induce the aligning of the dislocation line in effective [132] and [143] directions. The illustrated concept was supported by MD simulations in the configuration shown in Fig. 5d. We performed MD simulations for a dislocation line along the $\langle \bar{1}01 \rangle$ direction, close to the surface. We noticed that the dislocation line starts bending towards the normal to the surface. Obviously, in order to observe the completion of this process down to the bottom part of the simulation cell, much larger simulation times would be required.

It should be also noted that the dislocations terminating the stacking fault on the left and right in Fig. 5d, have different terminations, namely with silicon (on the left) and carbon (on the right) atoms. Nevertheless, the character of the evolution of both dislocations forming the $\langle 011 \rangle$ / $\langle 121 \rangle$ stepping of the dislocation lines, remains the same. We conclude therefore that the mechanism of the formation of the unusual $\langle 132 \rangle$ and $\langle 143 \rangle$ dislocation line directions is not related to the differences in the velocities of the dislocation segments with different core atom types.

Let's now summarize schematically the findings obtained by TEM and MD simulations. Fig. 5e represents our situation in the plane (111). Black $\langle \bar{1}10 \rangle$ lines are the intersections of the lamellae faces with the (111) plane. Green, light blue, dark blue and magenta lines are the PDs that lie along with the $\langle 112 \rangle$, $\langle 123 \rangle$, $\langle 134 \rangle$ and $\langle 01\bar{1} \rangle$ direction respectively. Black thick arrows are the Burgers vectors in the (111) plane ($1/6\langle \bar{1}2\bar{1} \rangle$ and $1/6\langle 11\bar{2} \rangle$). The PD on the left (green) has the shorter line connecting the lamellae faces along the (111) plane and has the Burgers vector ($1/6\langle \bar{1}2\bar{1} \rangle$) titled 60° respect the line direction. The other PD, on the right, has Burgers vector of $1/6\langle 11\bar{2} \rangle$ and line directions that can be either $\langle 01\bar{1} \rangle$ (magenta), $\langle 13\bar{4} \rangle$ (blue) or $\langle 12\bar{3} \rangle$ (light blue). As above reported, it can lower its length (and thus the energy) by using the $\langle 134 \rangle$ or $\langle 123 \rangle$ directions by realizing a zigzag structure by combining the $\langle 11\bar{2} \rangle$ and $\langle 01\bar{1} \rangle$ segments.

## 3.2. IDB structure

In this section, we report the experimental study of the structure of IDBs, lying in the {111} planes, with low and high-resolution scanning TEM. In Fig. 6, a cross-section STEM image shows an IDB at low resolution. In the insets of Fig. 6 (white squares), high-resolution images acquired on the left and on the right, with respect to the IDB, evidence that silicon and carbon in both regions are rotated each other. Here, silicon atoms have higher electron scattering cross-sections than carbon atoms, so that they are detectable as larger white halos, while smaller gray shoulders near Si indicate the C atoms. In the top-left inset, the C atoms of the Si-C diatoms are located above the Si atoms. On the contrary, Si atoms are above the C atoms in the right–down inset. A boundary develops between these two configurations. Complex white structures, visible in the middle of the image, are due to the 3D structure of the boundary. We remind that this image is a bi-dimensional projection of a three-dimensional boundary onto the (110) plane. Dispersed white regions with a complex structure indicate the places where the IDB does not lie in the plane perpendicular to the (110). In these regions, it is possible to find steps and disconnections. Indeed, there are many indications in the figures that smaller defects are present. Unfortunately, due to their 3D nature, they are not "fully" parallel to the electron beam direction: as an example of complex 3D structure, a three-dimensional intersection of an IDB and a SF$<2>$ with the presence of disconnections is shown in Fig. 7 S.I. The tridimensional nature of the boundary highly complicates the analyses. Nevertheless, the IDB structure can be unveiled when the IDB lying plane is perpendicular to the (110) plane, as it is found in the two regions highlighted with red squares and individuated with (1) and (2) in Fig. 6. In particular, in the region (1) the boundary lyes in the $(\bar{1}10)$ plane and in the region (2) in the $(\bar{1}1\bar{1})$ plane, respectively. Fine structures of the IBD in the regions (1) and (2) are shown in Figs. 8 S.I. and 7. Note that only in these portions, where the boundary is perpendicular to the (110) plane, it is possible to observe the internal structure of the boundary in the high-resolution STEM images.

The high-resolution image of the boundary in the region (2) of Fig. 6 is presented in Fig. 7 on the left, while on the right we show a sketch of its reconstruction. Two peculiarities are apparent about this IDB, namely: (i) it is coherent and (ii) it contains an intrinsic SF(SF$<1>$). In Fig. 7, the red arrows indicate the plane of the boundary, while the yellow arrow (and the yellowish region) indicate the plane of the SF$<1>$. The presence of SF$<1>$ is revealed by a shift in the positions of the C atoms at the Si-C dimers by the vector $1/6 <112>$ with respect to the crystal. The angle between the diatoms, adjacent to the boundary, and belonging to two different crystals, is about 70° and the bonds are almost undistorted.

In our investigation, we found that other kinds of IDBs are also possible. Two other examples are shown in Fig. 8 and Fig. 9 S.I. In Fig. 8, the IDB, lying along the $(\bar{1}11)$ plane is constituted by a Si-Si bound and a conservative SF (i.e. SF$<3>$). In the reconstruction presented on the right, the yellowish shaded region is the SF$<3>$. The red arrow represents the plane of the Si-Si bonds while the yellow arrow represents the coherent boundary of the SF$<3>$ with the rest of the crystal. Fig. 9 S.I shows an even more complex IDB configuration. In this image three SFs are associated with IDB. It is worth noting that all the IDBs lying in {111} planes, as observed up to now, are correlated with SFs and the number of SFs is odd.

Other crystals than 3C-SiC exhibit IDBs for example ZnO, AlN and GaAs, GaP, GaSb [46–48]. In all these materials, one lattice is related to the other by both a rotation of 180° and a small translation nevertheless the structures reported here are different from those reported in the literature [49,50]. An example of IDB structure can be found in Ref. [47] Fig. 3a and b for GaSb. The structure
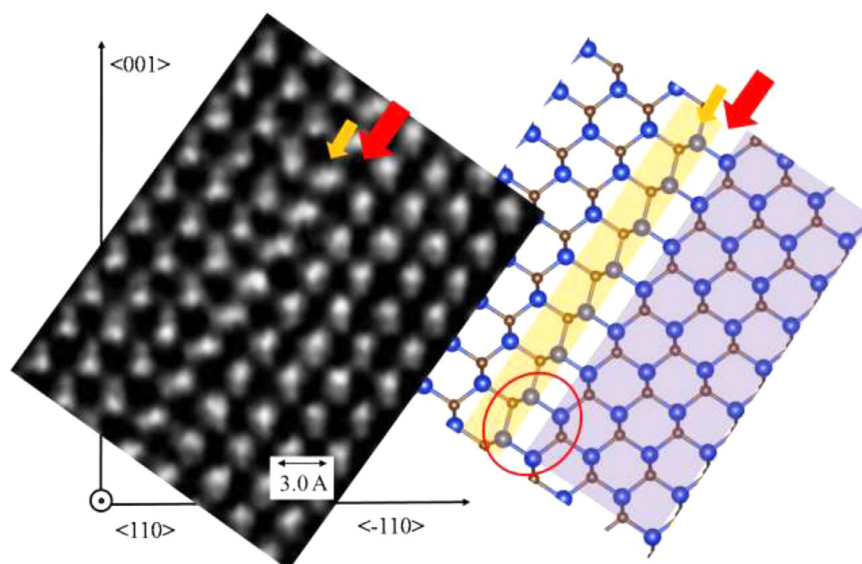
**Fig. 7.** IDB laying along the (1-11) plane observed in Fig. 6 region (2). High-resolution cross-section HAADF-STEM image on the left and reconstruction of the boundary on the right is shown. The yellowish shaded region in the reconstruction represents the SF<1> associated with the IDB. The red arrow represents the plane of the Si-Si bond while the yellow arrow represents the position of the SF<1> associated with the IDB. (For interpretation of the references to color in this figure legend, the reader is referred to the web version of this article.)
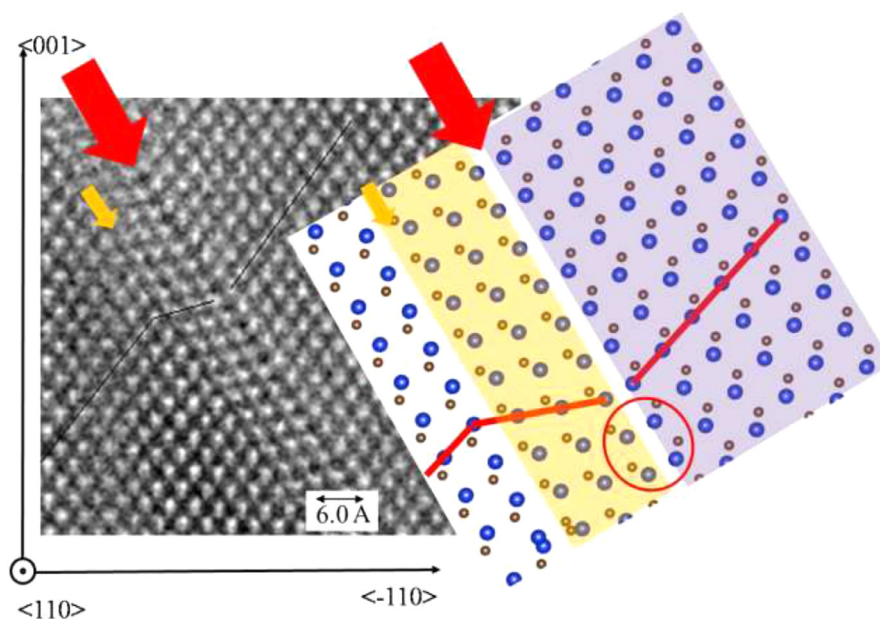


**Fig. 8.** High-resolution bright-field -STEM image of an IDB laying along the ($\bar{1}$11) plane and its reconstruction on the right. The yellowish shaded region in the reconstruction represents the SF<3> associated with the IDB. The red arrow represents the plane of the Si-Si bond while the yellow arrow represents the end of the SF<3> associated with the IDB. (For interpretation of the references to color in this figure legend, the reader is referred to the web version of this article.)

found in the present article resembles the "coherent mirror twin boundary" already shown in Ref. [47] (Fig. 2b in SiC and 2c for GaAs), indeed, the peculiar distorted hexagonal structure of a twin, highlighted with a red circle in Fig. 7–9 S.I., is apparent. Moreover, here, an additional SF (a further shift in the crystal structure) has to be introduced to couple the two inverted crystals. Twin boundary is very common in SiC due to low interface energy and its presence, associated with an SF (or an odd number of SFs), can realize a very low-energy structure able to couple two inverted crystals.

The copresence of SFs associated with a coherent twin realizing, the IDB, could give some insight into the formation of SFs in 3C-SiC. As reported by Han et al. and the references therein, lattice dislocations (perfect or partial) and SFs can be emitted (or adsorbed) from (grain or) domain boundaries under applied stress leaving a disconnection on the boundary [24–27,35,36,45]. Indeed, for strictly topological reasons, both perfect and PDs have to "start" and to "end" on crystal surfaces. Moreover, it was recently demonstrated that the SFs (and PDs) in 3C-SiC can be generated during growth on the IDB due to interface instability [51]. This fact allows us to also speculate on the formation of SFs in 3C-SiC at IDB. Actually, in the present paper, we observed that IDB in {111} planes has SFs intrinsically associated to the boundary. IDB can also lie on planes different from {111} planes, while SFs are always "anchored" to {111} planes. So we can speculate that when the IDB, during the growth, changes the location plane, these two defects could separate each other. So, once the IDB passes "through" the {111} plane, an SF could be emitted.

## 4. Conclusions

In conclusion, in this work, we analyzed by extensive STEM measurements the structure of extended defects in 3C-SiC. High-resolution STEM measurements allow us to have information on the structure of SFs and IDBs. Low-resolution plan-view TEM images show that PDs, can also display anomalous lie in non-conventional line directions: [112], [123] and 134]. A TEM analysis in, "two-beam configuration", shows that the angle between the Burger vectors and the dislocation line directions are 60° or are comprised between 0 and 30°. These considerations allow us to simulate the structure by using a molecular dynamic approach. The simulations show that [110] and [112] directions are stable, while the appearing and weird [123] and [134] directions should be a convolution of zigzag segments along the common [112] and [110] directions.

We also investigate the structure of IDB lying in along the (111) plane at very high resolution, to highlight the very nature of IDBs. In particular, we found that IDB lying along the (111) plane is composed of a Si-Si bound and an odd number of SFs. This structure allows having undistorted bound minimizing the interface energy. SF, associated with the IDB on (111), can be either intrinsic, extrinsic, or conservative. We also speculate that such a structure could realize the "seed" for the nucleation of the SFs.

## Declaration of Competing Interest

The authors declare that they have no known competing financial interests or personal relationships that could have appeared to influence the work reported in this paper.

## Acknowledgments

## Supplementary materials

Supplementary material associated with this article can be found, in the online version, at doi:10.1016/j.actamat.2021.116915.

## References

[1] F. La Via, A. Severino, R. Anzalone, C. Bongiorno, G. Litrico, M. Mauceri, M. Schoeler, P. Schuh, P. Wellmann, From thin film to bulk 3C-SiC growth: understanding the mechanism of defects reduction, Mater. Sci. Semiconduct. Process. 78 (2018) 57–68.

[2] T. Yasuda, M. Kato, M. Ichimura, T. Hatayama, SiC photoelectrodes for a self–driven water-splitting cell, Appl. Phys. Lett. 101 (2012) 053902.

[3] M. Kato, T. Yasuda, K. Miyake, M. Ichimura, T. Hatayama, Epitaxial p-type SiC as a self-driven photocathode for water splitting, Int. J. Hydrog. Energy 39 (10) (2014) 4845–4849.

[4] Q.B. Ma, B. Kaiser, J. Ziegler, D. Fertig, W. Jaegermann, XPS characterization and photoelectrochemical behaviour of p-type 3C-SiC films on p-Si substrates for solar water splitting, J. Phys. D Appl. Phys. 45 (32) (2012) 325101.

[5] C. He, X. Wu, J. Shen, P.K. Chu, High-efficiency electrochemical hydrogen evolution based on surface autocatalytic effect of ultrathin 3C-SiC nanocrystals, Nano Lett. 12 (3) (2012) 1545–1548.

[6] J. Jian, Y. Shi, S. Ekeroth, J. Keraudy, M. Syväjärvi, R. Yakimova, U. Helmersson, J. Sun, A nanostructured NiO/cubic SiC p–n heterojunction photoanode for enhanced solar water splitting, J. Mater. Chem. A 7 (2019) 4721–4728.

[7] M. Bhatnagar, B.J. Baliga, Comparison of 6H-SiC, 3C-SiC, and Si for power devices, IEEE Trans. Electron Devices 40 (3) (1993) 645–655.

[8] G.L. Harris, Properties of Silicon Carbide, Institution of Electrical Engineers, London, UK, 1995.

[9] F. Ciobanu, G. Pensl, H. Nagasawa, A. Schoner, S. Dimitrijev, K.Y. Cheong, V.V. Afanas'ev, G. Wagner, Traps at the interface of 3C-SiC/SiO2-MOS-structures, Mater. Sci. Forum 433-436 (2003) 551–554.

[10] S.E. Saddow, A. Agarwal, Advances in Silicon Carbide Processing and Applications, Artech House Publisher, Boston, MA, USA, 2004.

[11] Steven E. Saddow (Ed.), Silicon Carbide Biotechnology Elsevier, 2016 Editor.

[12] R. Anzalone, S. Privitera, M. Camarda, A. Alberti, G. Mannino, P. Fiorenza, S. Di Franco, F. La Via, Interface state density evaluation of high quality hetero-epitaxial 3C–SiC(0 0 1) for high-power MOSFET applications, Mater. Sci. Eng. B 198 (2015) 14–19.

[13] T. Kimoto, J.A. Cooper, Fundamental of Silicon Carbide, Technology IEEE Wiley, 2014.

[14] F. La Via, F. Roccaforte, A. La Magna, R. Nipoti, F. Mancarella, P. Wellman, D. Crippa, M. Mauceri, P. Ward, L. Miglio, M. Zielinski, A. Schöner, A. Nejim, L. Vivani, R. Yakimova, M. Syväjärvi, G. Grosset, F. Torregrossa, M. Jennings, P. Mawby, R. Anzalone, S. Coffa, H. Nagasawa, 3C-SiC hetero-epitaxially grown on silicon compliance substrates and new 3C-SiC substrates for sustainable wide-band-gap power devices (CHALLENGE), Mater. Sci. Forum 924 (2018) 913–918.

[15] G. Ferro, 3C-SiC heteroepitaxial growth on silicon: the quest for holy grail, Crit. Rev. Solid State Mater. Sci. 40 (1) (2015) 56–76.

[16] A.A. Lebedev, P.L. Abramov, S.P. Lebedev, G.A. Oganesyan, A.S. Tregubova, D.V. Shamshur, Influence of the defect density (twins boundaries) on electrical parameters of 3C-SiC epitaxial films, Phys. B 404 (2009) 4758–4760.

[17] H. Nagasawa, K. Yagi, T. Kawahara, N. Hatta, Reducing planar defects in 3C–SiC, Chem. Vap. Depos. 12 (2006) 502–508.

[18] H. Nagasawa, K. Yagi, T. Kawahara, 3C-SiC hetero-epitaxial growth on undulant Si(0 0 1) substrate, J. Cryst. Growth 237–239 (2002) 1244–1249.

[19] F. Giannazzo, G. Greco, S. Di Franco, P. Fiorenza, I. Deretzis, A. La Magna, C. Bongiorno, M. Zimbone, F. La Via, M. Zielinski, F. Roccaforte;, Impact of stacking faults and domain boundaries on the electronic transport in cubic silicon carbide probed by conductive atomic force microscopy, Adv. Electron. Mater. 6 (2020) 1901171.

[20] E. Scalise, L. Barbisan, A. Sarikov, F. Montalenti, L. Miglio, A. Marzegalli, The origin and nature of killer defects in 3C-SiC for power electronic applications by a multiscale atomistic approach, J. Mater. Chem. C 8 (2020) 8380–8392.

[21] X. Song, J.F. Michaud, F. Cayrel, M. Zielinski, M. Portail, T. Chassagne, E. Collard, D. Alquier, Evidence of electrical activity of extended defects in 3C-SiC grown on Si, Appl. Phys. Lett. 96 (2010) 142104.

[22] M. Zimbone, E.G. Barbagiovanni, C. Bongiorno, C. Calabretta, L. Calcagno, G. Fisicaro, A. La Magna, F. La Via, Generation and termination of stacking faults by inverted domain boundaries in 3C-SiC, Cryst. Growth Des. 20 (2020) 3104–3111.

[23] J. Yamasaki, S. Inamoto, Y. Nomura, H. Tamaki, N. Tanaka, Atomic structure analysis of stacking faults and misfit dislocations at 3C-SiC/Si(0 0 1) interfaces by aberration-corrected transmission electron microscopy, J. Phys. D Appl. Phys. 45 (2012) 49.

[24] L. Zou, C. Yang, Y. Lei, D. Zakharov, J.M.K. Wiezorek, D. Su, Q. Yin, J. Li, Z. Liu, E.A. Stach, J.C. Yang, L. Qi, G. Wang, G. Zhou;, Dislocation nucleation facilitated by atomic segregation, Nat. Mater. 17 (2018) 56–63.

[25] J.D. Rittner, D.N. Seidman, K.L. Merkle, Grain-boundary dissociation by the emission of stacking faults Lomer dislocation, Phys. Rev. B 53 (8) (1996).

[26] V. Borovikov, M.I. Mendelev, AH. King, Effects of solutes on dislocation nucleation from grain boundaries, Int. J. Plast. 90 (2017) 146–155.

[27] J. Han, S.L. Thomas, D.J. Srolovitz, Grain-boundary kinetics: a unified approach, Prog. Mater. Sci. 98 (2018) 386–476.

[28] H. Sternlicht, W. Rheinheimer, A. Mehlmanna, A. Rothschild, M.J. Hoffmann, W.D. Kaplan, The mechanism of grain growth at general grain boundaries in SrTiO3, Scr. Mater. 188 (2020) 206–211 November.

[29] H. Sternlicht, W. Rheinheimer, M.J. Hoffmann, W.D. Kaplan, The mechanism of grain boundary motion in SrTiO3, J. Mater. Sci. 51 (2016) 467–475.

[30] G. Litrico, R. Anzalone, A. Alberti, C. Bongiorno, G. Nicotra, M. Zimbone, M. Mauceri, S. Coffa, F. La Via, Stacking faults defects on 3C-SiC homo-epitaxial films, Mater. Sci. Forum 924 (2018) 124–127.

[31] M. Marinova, F. Mercier, A. Mantzari, I. Galben, D. Chaussende, E.K. Polychroniadis, A TEM study of in-grown stacking faults in 3C-SiC layers grown by CF-PVT on 4H-SiC substrates, Phys. B Condens. Matter 404 (23–24) (2009) 4749–4751 Volume.

[32] U. Lindefelt, H. Iwata, S. Öberg, P.R. Briddon, Stacking faults in 3C–,4H–, and 6H–SiC polytypes investigated by an ab initio supercell method, Phys. Rev. B 67 (2003) 155204.

[33] G. Litrico, R. Anzalone, A. Alberti, C. Bongiorno, G. Nicotra, M. Zimbone, M. Mauceri, S. Coffa, F. La Via, Stacking faults defects on 3C-SiC homo-epitaxial films, Mater. Sci. Forum 924 (2018) 124–127.

[34] M. Marinova, F. Mercier, A. Mantzari, I. Galben, D. Chaussende, E.K. Polychroniadis, A TEM study of in-grown stacking faults in 3C-SiC layers grown by CF-PVT on 4H-SiC substrates, Phys. B Condens. Matter 404 (23–24) (2009) 4749–4751.

[35] A. Sarikov, A. Marzegalli, L. Barbisan, F. Montalenti, L. Miglio, Structure and stability of partial dislocation complexes in 3C-SiC by molecular dynamics simulations, Materials 12 (2019) 3027.

[36] U. Lindefelt, H. Iwata, S. Öberg, P.R. Briddon, Stacking faults in 3C–,4H–, and 6H–SiC polytypes investigated by an ab initio supercell method, Phys. Rev. B 67 (2003) 155204.

[37] J.P. Hirth, J. Lothe, Theory of Dislocations, Wiley, New York, 1982 (1982).

[38] D. Hull, D.J. Bacon, Introduction to Dislocations, Fifth Ed., Elsevier, 2011.

[39] M. Lancin, M. Texier, G. Regula, B. Pichaud, Defects created in N-doped 4H-SiC in the brittle regime: Stacking fault multiplicity and dislocation cores, Philos. Mag. 89 (15) (2009) 1251–1266, doi:10.1080/14786430902919497.

[40] M. Zimbone, M. Mauceri, G. Litrico, E.G. Barbagiovanni, C. Bongiorno, F. La Via, Protrusions reduction in 3C-SiC thin film on Si, J. Cryst. Growth 498 (2018) 248–257.

[41] A. Severino, G. D'Arrigo, C. Bongiorno, S. Scalese, F.La Via, G. Foti, Thin crystalline 3C-SiC layer growth through carbonization of differently oriented Si substrates, J. Appl. Phys. 102 (2007) 023518.

[42] R. Anzalone, A. Severino, G. D'Arrigo, C. Bongiorno, G. Abbondanza, G. Foti, S. Saddow, F. La Via, Heteroepitaxy of 3C-SiC on different on-axis oriented silicon substrates, J. Appl. Phys. 105 (2009) 084910.

[43] S. Plimpton, Fast parallel algorithms for short-range molecular dynamics, J. Comput. Phys. 117 (1995) 1–19.

[44] P. Erhart, K. Albe, Analytical potential for atomistic simulations of silicon, carbon, and silicon carbide, Phys. Rev. B 71 (2005) 035211.

[45] A. Sarikov, A. Marzegalli, L. Barbisan, E. Scalise, F. Montalenti, L. Miglio, Molecular dynamics simulations of extended defects and their evolution in 3C-SiC by different potentials, Model. Simul. Mater. Sci. Eng. 28 (2020) 015002.

[46] A. Stukowski, Visualization and analysis of atomistic simulation data with OVITO–the open visualization tool Model, Simul. Mater. Sci. Eng. 18 (2010) 015012.

[47] K. Momma, F. Izumi, VESTA 3 for three-dimensional visualization of crystal, volumetric and morphology data, J. Appl. Crystallogr. 44 (2011) 1272–1276.

[48] D.B. Williams, C.B. Carter, Transmission Electron Microscopy: A Textbook for Materials Science, Springer, 2009.

[49] Y.A.R. Dasilva, R. Kozak, R. Erni, M.D. Rossell, Structural defects in cubic semiconductors characterized by aberration-corrected scanning transmission electron microscopy, Ultramicroscopy 176 (2017) 11–22.

[50] O. Rubel, S.D. Baranovskii, Formation energies of antiphase boundaries in GaAs and GaP: an *ab initio* study, Int. J. Mol. Sci. 10 (12) (2009) 5104–5114.

[51] G. Fisicaro, C. Bongiorno, I. Deretzis, F. Giannazzo, F. La Via, F. Roccaforte, M. Zielinski, M. Zimbone, A. La Magna, Genesis and evolution of extended defects: the role of evolving interface instabilities in cubic SiC, Appl. Phys. Rev. 7 (2020) 021402.